Supplement of Atmos. Chem. Phys., 23, 9023–9036, 2023
https://doi.org/10.5194/acp-23-9023-2023-supplement
© Author(s) 2023. CC BY 4.0 License.

Atmospheric Chemistry and Physics
Open Access
EGU

*Supplement of*

# Nighttime NO emissions strongly suppress chlorine and nitrate radical formation during the winter in Delhi

**Sophie L. Haslett et al.**

*Correspondence to:* Claudia Mohr (claudia.mohr@psi.ch), Sachchida N. Tripathi (snt@iitk.ac.in), and Sophie L. Haslett (sophie.haslett@aces.su.se)

The copyright of individual parts of the supplement might differ from the article licence.

## 1 Supplementary text

### S1 Quantification of the $N_2O_5$ signal in the FIGAERO-CIMS

The quantification of the $IN_2O_5^-$ signal at *m/z* 234.886 was established using chamber experiments, which were carried out at the Paul Scherrer Institute (PSI) using the same instrument. These will be the subject of another publication. In brief, a Teflon chamber (Platt et al., 2014, 2017; Bruns et al., 2015) was filled with zero air generated from an zero air generator (AADCO) and a series of injections of $NO_2$ and $O_3$ were performed (without lights on), allowing $N_2O_5$ molecules to form. The concentrations of NO, $NO_2$ (Thermo 42C) and $O_3$ (Thermo 49C) were measured independently, while the gas-phase $N_2O_5$ concentrations were measured using the FIGAERO-CIMS. The relative humidity in the chamber was around 80%, which is comparable with values that were encountered during the field campaign in Delhi. During these measurements, polonium-210 ($^{210}$Po) was used as an ioniser and the IMR was set to a pressure of 100 mbar.

We used the simplified box model described below to simulate $N_2O_5$ formation in the chamber. In the model setup, NO, $NO_2$ and $O_3$ parameters were input to the model as known values. Lights were kept off, so there was no photolysis parameter. All loss terms were combined into a single parameter, $k_{N2O5}$, which was unknown. Different values for $k_{N2O5}$ were tested. For each tested value of $k_{N2O5}$, the modelled value of $N_2O_5$, averaged to 5 s intervals, was plotted against the $N_2O_5$ signal from the CIMS, a regression line was fitted and the $r^2$ parameter was found. In each case, the simulated concentrations of $N_2O_5$ were then used to estimate the sensitivity of the FIGAERO-CIMS according to the best fit line. This estimated sensitivity was plotted against the $r^2$ parameter and the sensitivity at the maximum value of $r^2$ was used to calibrate the $N_2O_5$ data. A loss term of 0.004 $s^{-1}$ was selected, as this demonstrated the best fit (Figs. S7, S8). This method yielded a sensitivity of 10.2 cps $pptv^{-1}$ per million counts of iodide.

During the Delhi campaign, an X-ray ioniser was used and the IMR pressure was set to 250 mbar. In order to increase transmission efficiency, a number of the voltages in the instrument were also changed. Using the chamber, we established a conversion rate for the instrument sensitivity by swapping between the $^{210}$Po ionisation source and the X-ray ioniser and changing the voltages, during periods when the quantity of NO, $NO_2$, $O_3$ and thus $N_2O_5$ in the chamber were steady. This comparison yielded a conversion factor of 5.3 between the $N_2O_5$ signal measured using the $^{210}$Po ionisation source and that using the X-ray ioniser (Fig. S9). In total, this process suggests an overall sensitivity of 54 cps $pptv^{-1}$ for the Delhi measurements. The calibration factors for chlorine-containing compounds measured by the FIGAERO-CIMS ($ClNO_2$, $Cl_2$, Cl, $ClONO_2$ and HOCl) are assumed to be the same as for $N_2O_5$, given that a number of previous studies have found very similar calibration factors between $N_2O_5$ and $ClNO_2$ (Tham et al., 2016; Zhou et al., 2018; Wang et al., 2017).

This empirically determined sensitivity was compared with the theoretical maximum sensitivity, as established by Lopez-Hilfiker et al., (2016). It has been found that the maximum sensitivity for the CIMS at the collision limit for iodide adduct chemistry is 22 cps $pptv^{-1}$ per million counts of iodide (Lopez-Hilfiker et al., 2016) and an IMR pressure of 100 mbar. This figure was established using $N_2O_5$, as it is known to react with $I^-$ at the collision limit (Huey et al., 1995).

There are two routes through which $N_2O_5$ interacts with $I^-$: it either creates the iodide-adduct with the parent ion at *m/z* 234.886 ($I\text{-}N_2O_5^-$), or reacts to form $NO_3^-$, which is detected at *m/z* 61.988, and $I\text{-}NO_2$, which is not detected by the CIMS. The value of 22 cps $pptv^{-1}$ was established using the sum of both pathways, with *m/z* 234.886 contributing just under a third of the total signal. This gives an estimated maximum sensitivity of approximately 7 cps $pptv^{-1}$ from the *m/z* 234.886 peak alone, which is the reference case with which our instrumental setup will be compared.

The value of 22 cps $pptv^{-1}$ was found using $^{210}Po$ to ionise the iodide and an $I^-$ flow rate of 2 lpm. Using $^{210}Po$ produced around 60 times more $I^-$ when compared with the X-ray ioniser in our chamber experiments. In order to increase instrument sensitivity when using the X-ray ioniser, we increased the pressure inside the IMR from 100 mbar, as was used with $^{210}Po$ as an ioniser, to 250 mbar. In addition, the flow rate of $I^-$ into the IMR when using the X-ray ioniser was reduced to 1.5 lpm.

The maximum kinetically limited sensitivity, $S_{kin}^{typ}$, in units of counts per second/pptv/million reagent ions ($I^-$) for the CIMS can be found using Eq. S1.

$$S_{kin}^{typ} = \frac{10^6[\mathrm{M}]_{\mathrm{IMR}} f k_{coll} t_{\mathrm{IMR}}}{10^{12}} \quad \text{(S1)}$$

Where $[\mathrm{M}]_{\mathrm{IMR}}$ represents the number density inside the IMR, $f$ is the fraction of flow into the IMR that is made up by the sample flow, and $t_{IMR}$ is the residence time of ions in the IMR (Bi et al., 2021).

The value of $f$ can be represented by Eq. S2

$$f = \frac{Q_{samp}}{Q_{samp}+Q_{I^-}} \quad \text{(S2)}$$

Where $Q_{samp}$ is the sample flow rate and $Q_{I^-}$ is the iodide reagent flow rate into the IMR (Bi et al., 2021). During our campaign, $Q_{samp}$ was the same as for the reference case. However, $Q_{I^-}$ was 25% smaller, resulting in the sample flow making up a larger fraction of the flow into the IMR. The difference can be calculated by substituting the flow rates into Eq. S2:

$$f^{Delhi} = \left(\frac{2\ \mathrm{lpm}}{2+1.5\ \mathrm{lpm}} \div \frac{2\ \mathrm{lpm}}{2+2\ \mathrm{lpm}}\right) f^0 = \frac{8}{7} f^0 \quad \text{(S3)}$$

Where $f^0$ refers to the reference case and $f^{Delhi}$ to results presented here.

Similarly, the residence time within the IMR, $t_{IMR}$, is influenced by both the iodide flow rate and the pressure inside the IMR, $P_{IMR}$, according to Eq. S4 (Bi et al., 2021):

$$t_{IMR} = \frac{V_{IMR}}{(Q_{samp}+Q_{I^-})\frac{P^{STP}}{P_{IMR}}} \quad \text{(S4)}$$

Where $V_{IMR}$ is the volume of the IMR and $P^{STP}$ is standard pressure. In this case, $Q_{I^-}$ is 25% smaller and $P_{IMR}$ is 2.5 times larger than in the reference case. Thus, the IMR residence time can be calculated from the reference case according to Eq. S5:

$$t_{IMR}^{Delhi} = \left( \frac{1}{\left(\frac{1.5+2\,\text{lpm}}{2+2\,\text{lpm}}\right)} \cdot \frac{1}{\left(\frac{1}{250\,\text{mbar}/100\,\text{mbar}}\right)} \right) t_{IMR}^{0} = \frac{20}{7} t_{IMR}^{0} \quad \text{(S5)}$$

From combining Eqs S1, S3 and S5, the maximum sensitivity $S^{Delhi}$ of our setup can be calculated from the reference case sensitivity ($S^0$) according to Eq. S6.

$$S^{Delhi} = 3.3\, S^0 \quad \text{(S6)}$$

This yields an estimated maximum sensitivity of 23 cps pptv$^{-1}$ per million $I^-$ counts for the FIGAERO-CIMS using the X-ray ioniser, with an iodide flow of 1.5 lpm and an IMR pressure of 250 mbar. Previous studies indicate that the sensitivity of the $IN_2O_5^-$ signal at *m/z* 234.886 and the $ICINO_2^-$ signal at *m/z* 207.867 will be influenced by the relative humidity within the instrument (Kercher et al., 2009; Dörich et al., 2021; Lee et al., 2014). During the campaign, the $IH_2O^-$ signal observed by the FIGAERO-CIMS during gas-phase measurements was around 13% of the iodide signal. This suggests a mixing ratio of approximately 0.69 g kg$^{-1}$ or a vapour pressure of 0.51 Torr within the IMR region (Dörich et al., 2021). It is therefore likely that, according to the results of laboratory experiments carried out by Kercher et al. (2009), this theoretically-estimated maximum sensitivity of 23 cps pptv$^{-1}$ per million $I^-$ counts is around three times too low for $N_2O_5$. Correcting for this yields a maximum sensitivity of 69 cps pptv$^{-1}$ per million $I^-$ counts under our measurement conditions, which corresponds well to our empirical estimate of 54 cps pptv$^{-1}$ from the chamber calculations. Here, we use the calibration value of 54 cps pptv$^{-1}$, including error bars of ±15 cps pptv$^{-1}$.

## S2 Additional information on the 0-dimensional box model calculations

### a. Reaction rate calculations for VOCs

In order to establish the loss rate of $NO_3$ from reactions with VOCs, the reaction rate of $NO_3$ with individual VOCs, and the relevant VOC's atmospheric concentration, is required. Here, reaction rates of $NO_3$ with different VOCs were taken from

Atkinson et al. (2006), at an assumed temperature of 298 K. Several different isomers for each molecular composition are listed, each with slightly different reaction rates with $NO_3$. As the PTR was unable to distinguish between different isomers, an estimate of the reaction rate for each molecular composition was established here by calculating the mean of all isomers with the given composition. The overall loss rate per molecular composition is then calculated by averaging the product of each isomer's reaction rate constant and its concentration in molecules $cm^{-3}$ (R5 in table S1). The individual isomers included in this calculation, and the calculated average reaction rate for each VOC chemical composition, are listed in Table S3.

**b. Wet aerosol surface area**

The SMPS provided binned measurements of dry fine aerosol number concentratiosn between 19 nm and 1 µm. These values were used to establish the average aerosol surface area per time step for each bin. A simple growth factor model was applied (Haslett et al., 2019) to calculate the wet aerosol size distribution and surface area. In brief, this involved the use of a single-parameter approach (Petters and Kreidenweis, 2007) to estimate the hygroscopic growth factor of aerosols based on the average chemical composition observed by the AMS. A simple ion-pairing scheme (Gysel et al., 2007), which was expanded to include chloride, was used to calculate the relative contributions of different neutral salts based on observed ion concentrations. Using the known densities, $\kappa$ values (the single parameter that describes a particle's propensity to grow hygroscopically (Petters and Kreidenweis, 2007) and calculated concentrations for each neutral salt, organics and black carbon, a single value of $\kappa$ for the average aerosol particle was established. From this, the hygroscopic growth factor (HGF) could be calculated using Eqs. S7 and S8 (Haslett et al., 2019; Petters and Kreidenweis, 2007), which were solved iteratively.

$$\frac{\mathrm{RH}}{\exp\left(\frac{A}{D_d \mathrm{HGF}}\right)} = \frac{\mathrm{HGF}^3 - 1}{\mathrm{HGF}^3 - (1-\kappa)} \quad \text{(S7)}$$

Where

$$A = \frac{4\sigma_{s/a} M_W}{\mathrm{R}T\rho_W} \quad \text{(S8)}$$

Here, RH is the relative humidity expressed as a fraction, HGF is the hygroscopic growth factor (i.e., the multiplicative factor by which the diameter of each particle grows as a result of taking up water), $D_d$ is the dry particle diameter (µm), $\sigma_{s/a}$ is the surface tension at the solution-air interface assumed to be the one of water (0.072 J $m^2$), $M_W$ is the molar mass of water (18 g $mol^{-1}$), $R$ is the universal gas constant (8.314 J $K^{-1}$ $mol^{-1}$), $T$ is the absolute temperature in K and $\rho_W$ is the density of water (1 g $cm^{-3}$).

The new wet aerosol surface area was then summed across all wet bin sizes for each time step, producing a single value of wet aerosol surface area in $cm^2$ $cm^{-3}$. Given the size limits of the SMPS, this study has been unable to include heterogeneous uptake by coarse-mode particles and so the loss factors from R6, R6 and R7 are likely to present slight underestimations. Nevertheless, previous studies in the Delhi urban area suggest there is a minimal contribution towards the aerosol mass from coarse-mode particles (Srivastava and Jain, 2007). It is therefore likely that the estimate presented here is a reasonable approximation.

**c. The aerosol uptake of $N_2O_5$**

Molecules of $N_2O_5$ can be taken up by particles, where they are accommodated into the surface layer at the gas-aerosol interface (R6) (Thornton and Abbatt, 2005; Tham et al., 2018). Once in the aerosol surface layer, these molecules undergo reactions that result in either the production of nitric acid ($HNO_3$) or the gaseous compound nitryl chloride ($ClNO_2$) (Thornton and Abbatt, 2005; Tham et al., 2018). The rate at which $N_2O_5$ molecules are taken up at particle surfaces is governed by the uptake coefficient, $\gamma_{N2O5}$. This essentially represents the probability that any given $N_2O_5$ molecule will react at an aerosol surface. It is influenced by a range of factors, including the availability of aerosol surface area, the ambient relative humidity (RH), the temperature and the chemical composition of aerosol particles (Thornton and Abbatt, 2005).

The value of $\gamma_{N2O5}$ can vary dramatically depending on ambient conditions. Values are found within the range of 0.001 – 0.2 (Yan et al., 2019). The value increases when the particles contain more chloride and water, but decreases with larger quantities of $NO_3^-$ within the particles, as well as with organic coatings (Tham et al., 2018, p.20; Riedel et al., 2012; Bertram and Thornton, 2009). Several parameterisations have been devised to calculate $\gamma_{N2O5}$ based on laboratory experiments (Bertram and Thornton, 2009; Evans and Jacob, 2005; Anttila et al., 2006). Here, we use a parameterisation that specifically takes into account the impact of chloride on $N_2O_5$ uptake (Bertram and Thornton, 2009). While such parameterisations do not always capture ambient uptake coefficients perfectly and have been found in some cases to diverge from observed ambient values (Xia et al., 2019), they have often been used to provide reasonable approximations (Mielke et al., 2013). The value of $\gamma_{N2O5}$ is established here using Eq. 9 (Bertram and Thornton, 2009).

$$\gamma_{N_2O_5} = \frac{4}{c_{N_2O_5}} \frac{V}{S_A} K_H \beta (1 - e^{-\delta[H_2O]}) \left(1 - \frac{1}{\frac{k_3[H_2O]}{k_{2b}[NO_3^-]} + 1 + \frac{k_4[Cl^-]}{k_{2b}[NO_3^-]}}\right) \quad \text{(S9)}$$

Here, $V$ represents the particle volume concentration in $m^3\ m^{-3}$, which can be calculated from SMPS data. $S_A$ is the particle surface area in $m^2\ m^{-3}$. $K_H$ is the Henry's law constant for $N_2O_5$ (taken here to be 51 (Bertram and Thornton, 2009)) and is dimensionless. $\beta$ is $1.16 \times 10^{-6}$ $s^{-1}$ and $\delta$ is $1.3 \times 10^{-1}$ $M^{-1}$. These constants were established from laboratory experiments (Bertram and Thornton, 2009). The ratios of $k_3/k_{2b}$ and $k_4/k_{2b}$ are the ratios of the rate constants for $NO_3^-$ with respect to water and $Cl^-$, respectively. These were found to be $6.0 \times 10^{-2}$ and 29. The molecular speed for $N_2O_5$ is represented by $c_{N2O5}$. Square brackets represent the concentration of the given species in M: that is, moles of the substance per litre of aerosol material.

The calculated diel pattern of $\gamma_{N2O5}$ using the method outlined above falls between 0.03 in the late afternoon and 0.07 in the early mornings. This compares well with values of $\gamma_{N2O5}$ provided in the literature, which show values between 0.001 and 0.02 in North America, compared with slightly higher values between 0.01 and 0.1 in China, where particulate loading is generally higher (Tham et al., 2018). The loss rate of $N_2O_5$ onto particle surfaces can then be established using the reaction rate shown for R6(Tham et al., 2018).

**d. Photolysis rate calculations**

The photolysis rate for a given compound is calculated using Eq. S10, where $j_i$ is the photolysis rate for compound $i$, $F_i(\lambda)$ is the actinic flux (photons per unit area), $\varphi_i(\lambda)$ is the quantum yield and $\sigma_i(\lambda)$ is the absorption cross section. The photolysis rate is integrated across all solar wavelengths ($\lambda$).

$$j_i = \int F_i(\lambda)\ \phi_i(\lambda)\ \sigma_i(\lambda)\ d\lambda \quad \text{(S10)}$$

Values for the actinic flux and quantum yield for $O_3$ and $NO_2$ were taken from Atkinson et al. (2006) and integrated across the solar spectrum (Finlayson-Pitts and Pitts, 2000), which produced maximum photolysis rates with a solar zenith angle (SZA) of 0° of 5e-5 $s^{-1}$ for $O_3$ and 9e-3 $s^{-1}$ for $NO_2$. The recommended value of 0.206 $s^{-1}$ was used for the maximum photolysis rate of $NO_3$ (Atkinson et al., 2006). The photolysis rates at any given time of day were scaled using the observed incoming solar radiation.

## S2 Supplementary tables

**Table S1: Reactions included in the simple 0-D chemical box model used to estimate $N_2O_5$ concentrations.**

| Reaction | Reaction rate | Equation |
|---|---|---|
| $NO_2 + O_3 \rightarrow NO_3 + O_2$ | $k_1$ = 3.5e-17 $cm^3$ $molecule^{-1}$ $s^{-1}$ (Atkinson et al., 2004) | R1 |
| $NO_3 + NO_2 \rightarrow N_2O_5$ | $k_2$ = 1.9e-12 $cm^3$ $molecule^{-1}$ $s^{-1}$ (Atkinson et al., 2004) | R2 |
| $N_2O_5 \rightarrow NO_3 + NO_2$ | $k_2$' = 1.7e-2 $s^{-1}$ (Atkinson et al., 2004) | R2' |
| $NO_3 + NO \rightarrow 2\ NO_2$ | $k_3$ = 2.6e-11 $cm^3$ $molecule^{-1}$ $s^{-1}$ (Atkinson et al., 2004) | R3 |
| $NO_3 + h\nu \rightarrow NO_2 + O$ | $j_4$ = 0.19 $s^{-1}$ (scaled by insolation)(Atkinson et al., 2004) | R4 |
| $NO_3 + h\nu \rightarrow NO + O_2$ | $j_4$' = 0.016 $s^{-1}$ (scaled by insolation) (Atkinson et al., 2004) | R4' |
| $NO_3$ + VOC → products | $k_5 = \Sigma(k_{VOC,i}\ [VOC]_i)$ | R5 |
| $N_2O_5 \rightarrow 2HNO_3$ or $ClNO_2$ (het) | $k_6 = 0.25\ c_{N2O5}\ \gamma_{N2O5}\ S_A$ (Yan et al., 2019) | R6 |
| $NO_3$ → products (het) | $k_7 = 0.25\ c_{NO3}\ \gamma_{NO3}\ S_A$ | R7 |

**Table S2: Statistics for VOC input parameters in F0AM.**

| **Compound** | **Median (ppbv)** | **Mean (ppbv)** | **Std (ppbv)** |
|---|---|---|---|
| Alpha-pinene | 0.0718 | 0.0827 | 0.0282 |
| Benzene | 1.4325 | 1.4765 | 0.6996 |
| Ethyl-benzene | 0.7400 | 1.1855 | 0.8347 |
| Trimethyl-1,2,4-benzene | 0.3850 | 0.5923 | 0.3879 |
| Trimethyl-1,3,5-benzene | 0.6100 | 0.66750 | 0.1678 |
| Toluene | 1.4050 | 2.3527 | 1.5213 |
| $C_5H_8$ | 0.4644 | 0.5664 | 0.2499 |
| Phenol | 0.1900 | 0.2079 | 0.0878 |
| Cresol | 0.1275 | 0.1373 | 0.4093 |
| $C_2H_6$ | 12.2450 | 12.3952 | 3.2206 |
| $C_2H_4$ | 7.6600 | 8.1958 | 3.2021 |
| n-butane | 10.0625 | 12.7502 | 6.2286 |
| $C_3H_8$ | 12.5850 | 14.6648 | 5.5893 |
| Hexane | 0.6700 | 0.8096 | 0.3069 |

170

**Table S3: Isomers included in the calculation of $k_5$.**

| VOC | $k$ ($s^{-1}$) | Average $k$ ($s^{-1}$) |
|---|---|---|
| Benzene ($C_6H_6$) | 3.0e-17 | 3.0e-17 |
| Toluene ($C_7H_8$) | 7.0e-17 | 7.0e-17 |
| o-Xylene ($C_8H_{10}$) | 4.1e-16 | 4.4e-16 |
| m-Xylene ($C_8H_{10}$) | 2.6e-16 | |
| p-Xylene ($C_8H_{10}$) | 5.0e-16 | |
| Ethylbenzene ($C_8H_{10}$) | 6.0e-16 | |
| Isoprene ($C_5H_8$) | 7.0e-13 | 7.0e-13 |
| 4-ethyltoluene ($C_9H_{12}$) | 8.6e-16 | 1.4e-15 |
| 1,2,3-trimethylbenzene ($C_9H_{12}$) | 1.9e-15 | |
| 1,2,4-trimethylbenzene ($C_9H_{12}$) | 1.8e-15 | |
| 1,3,4-trimethylbenzene ($C_9H_{12}$) | 8.8e-16 | |

| | | |
|---|---|---|
| Camphene ($C_{10}H_{16}$) | 6.6e-13 | 3.4e-11 |
| 2-carene ($C_{10}H_{16}$) | 1.9e-11 | |
| 3-carene ($C_{10}H_{16}$) | 9.1e-12 | |
| Limonene ($C_{10}H_{16}$) | 1.2e-11 | |
| Alpha-phellandrene ($C_{10}H_{16}$) | 7.3e-11 | |
| Beta-phellandrene ($C_{10}H_{16}$) | 8.0e-12 | |
| Alpha-pinene ($C_{10}H_{16}$) | 6.2e-12 | |
| Beta-pinene ($C_{10}H_{16}$) | 2.5e-12 | |
| Sabinene ($C_{10}H_{16}$) | 1.0e-11 | |
| Alpha-terpinene ($C_{10}H_{16}$) | 1.4e-10 | |
| Gamma-terpinene ($C_{10}H_{16}$) | 2.9e-11 | |
| Terpinolene ($C_{10}H_{16}$) | 9.7e-11 | |

## 3 Supplementary figures

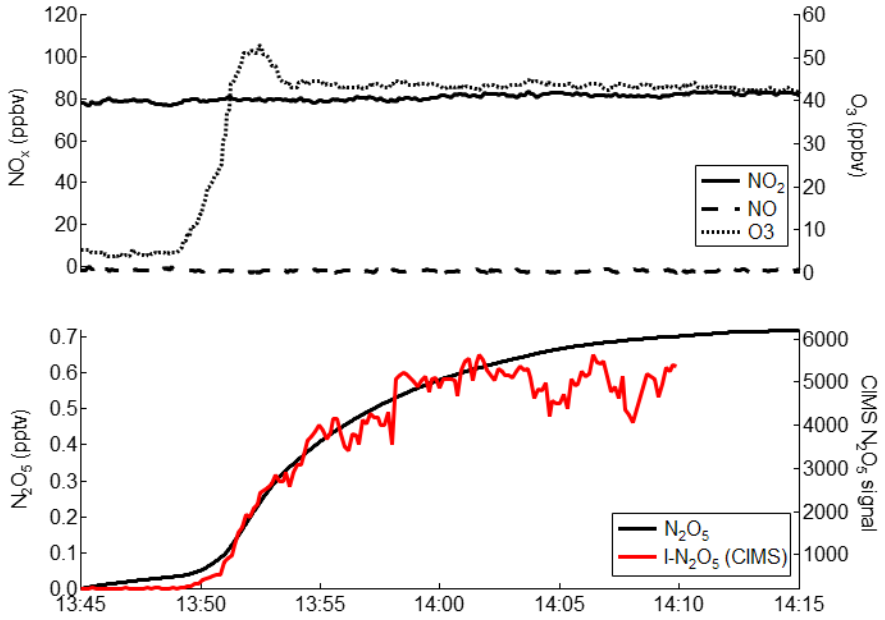

**Figure S1: Results from the chamber experiment, showing measured concentrations of NO, $NO_2$ and $O_3$ (in black in the top panel), along with the $N_2O_5$ signal measured by the FIGAERO-CIMS (red, lower panel) and the $N_2O_5$ and $NO_3$ concentrations in pptv predicted by the box model (black, lower panel).**

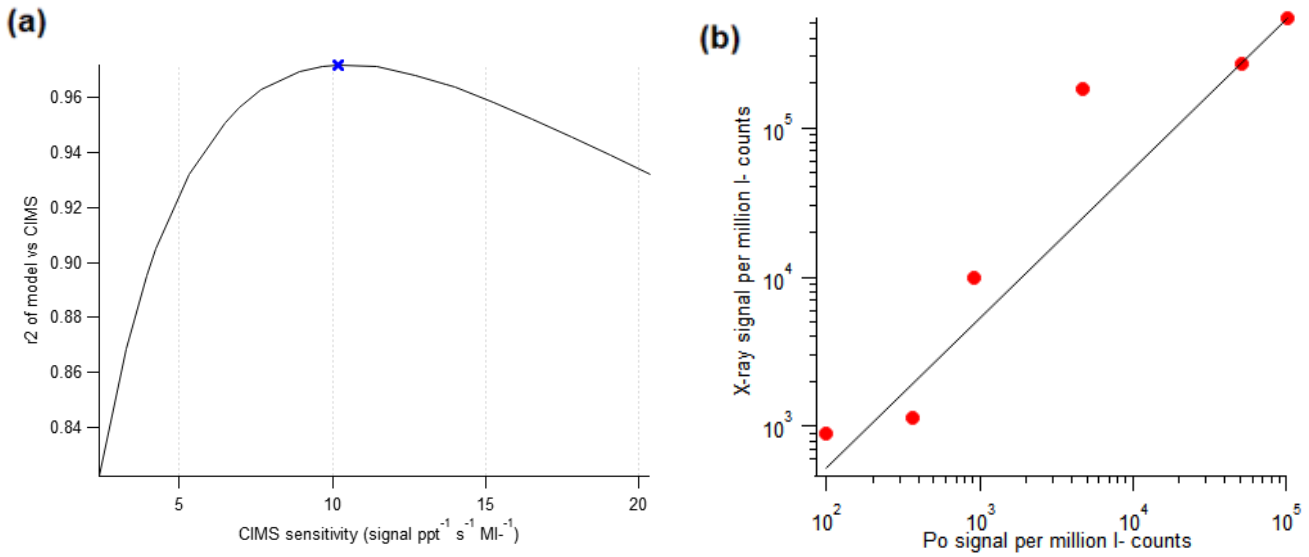


**Figure S2: An empirical estimate of the best sensitivity calibration factor to use with the FIGAERO-CIMS. (a) A plot of the regression value of the modelling results using different estimates for the CIMS sensitivity. The optimum fit is at a sensitivity of 10.2 $ppt^{-1}$ $s^{-1}$ $MI^{-1}$, shown here by the blue cross. (b) The relationship between the measured $N_2O_5$ signal using the X-ray ioniser vs the polonium ioniser.**

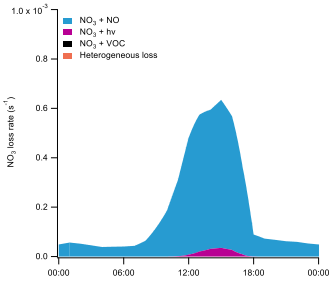


**Figure S3: The relative loss rates and pathways of $NO_3$ throughout the diel cycle.**

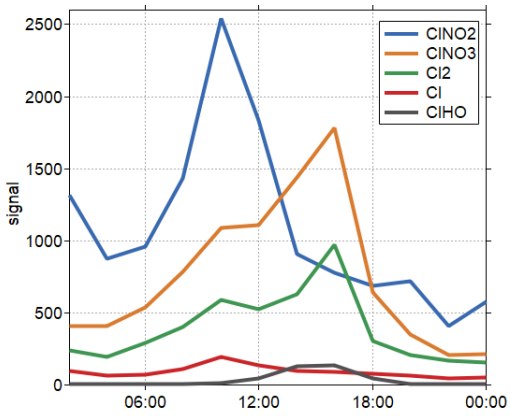


**Figure S4: A comparison of the signals observed from various chlorine-containing species. Each of these was observed with $I^-$. The signal from $ICl^-$ follows the $ICINO_2^-$ signal extremely closely, making it likely that this is an artefact of $ClNO_2$ measurements. The observed $ICINO_3^-$ signal is likely a combination of genuine ambient $ClONO_2$ and interactions between $ClNO_2$ and O in the IMR region.**

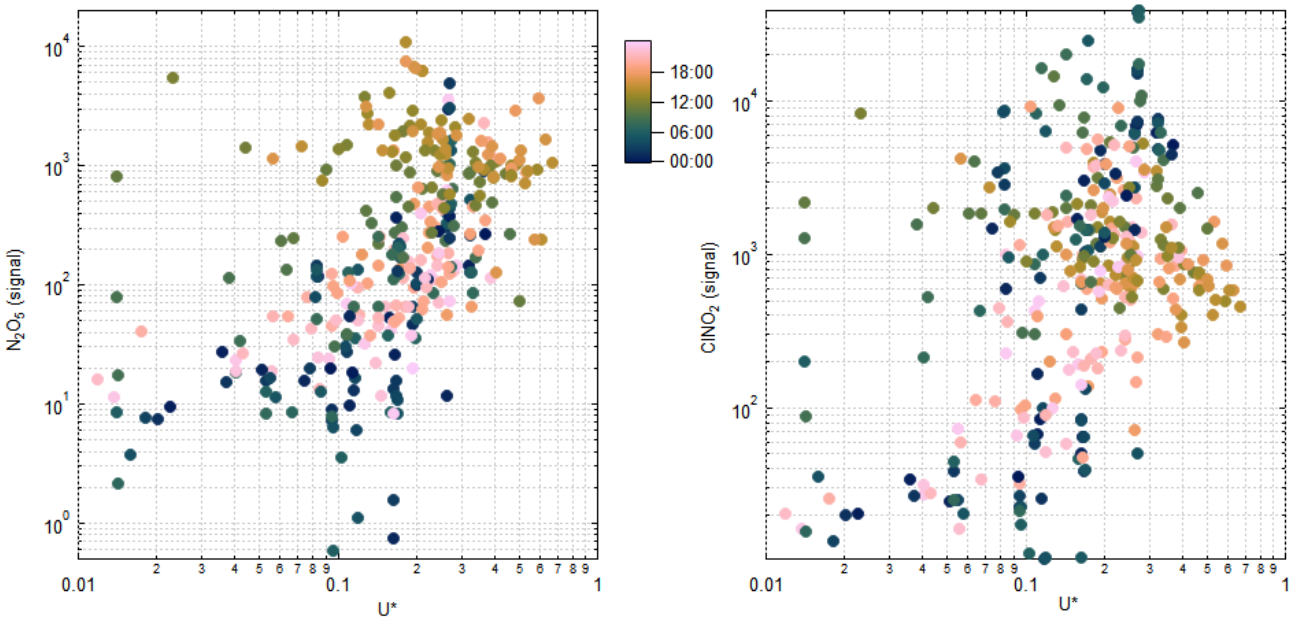


**Figure S5: A comparison of the $N_2O_5$ and $ClNO_2$ signals with friction velocity (U*), a value used as an indicator for atmospheric mixing. The increase in signal as mixing increases is consistent with here by a hypothesised source of these species in the residual layer, above the inlet.**

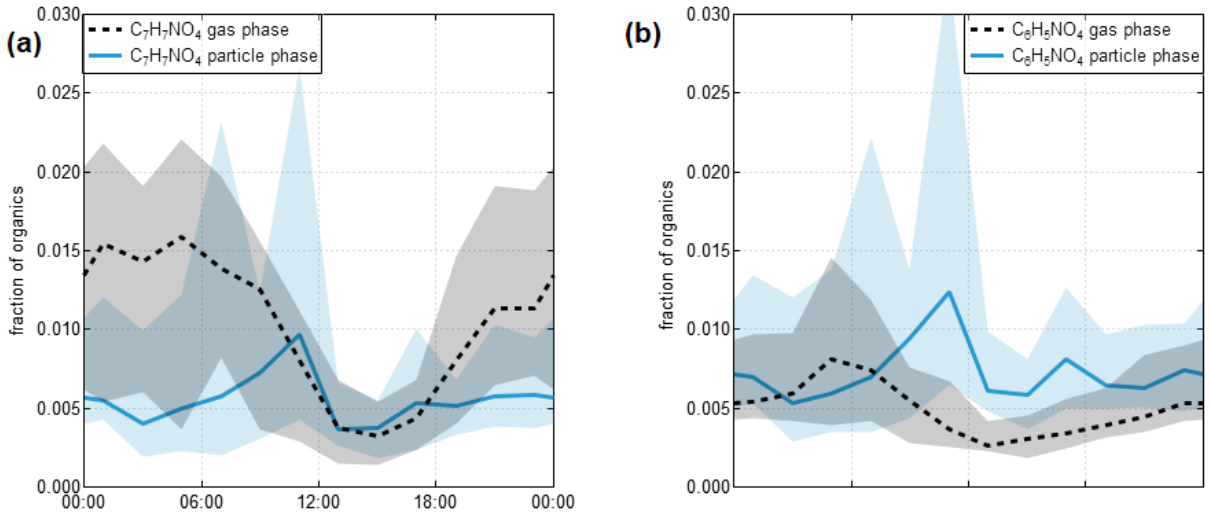


**Figure S6: Two examples of nitrogen-containing compounds that are often associated with biomass burning emissions. For both compounds, the contribution towards the gas phase decreases during the day, indicating that their likely emission sources are from biomass burning or other sources that have been shown to increase during the night, rather than from $NO_3$ oxidation.**

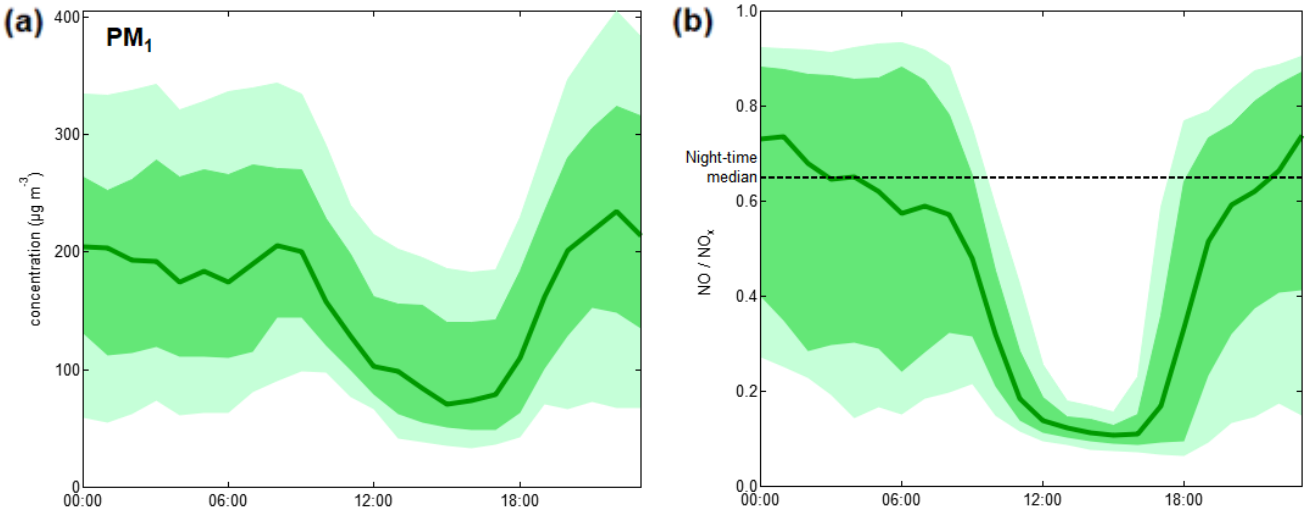


**Figure S7: Diel cycles observed during the campaign. (a) The summed diel cycle of all non-refractory $PM_1$ species (Organic compounds, $NO_3$, $SO_4$, $NH_4$ and chloride) as observed by the AMS (b) The diel cycle of the ratio of NO to total $NO_x$. The median night-time NO fraction is around 64% of total $NO_x$.**

**References**


Anttila, T., Kiendler-Scharr, A., Tillmann, R., and Mentel, T. F.: On the Reactive Uptake of Gaseous Compounds by Organic-Coated Aqueous Aerosols: Theoretical Analysis and Application to the Heterogeneous Hydrolysis of N2O5, J. Phys. Chem. A, 110, 10435–10443, https://doi.org/10.1021/jp062403c, 2006.

Atkinson, R., Baulch, D. L., Cox, R. A., Crowley, J. N., Hampson, R. F., Hynes, R. G., Jenkin, M. E., Rossi, M. J., and Troe, J.: Evaluated kinetic and photochemical data for atmospheric chemistry: Volume I - gas phase reactions of $O_x$, $HO_x$, $NO_x$ and $SO_x$ species, Atmospheric Chemistry and Physics, 4, 1461–1738, https://doi.org/10.5194/acp-4-1461-2004, 2004.

Atkinson, R., Baulch, D. L., Cox, R. A., Crowley, J. N., Hampson, R. F., Hynes, R. G., Jenkin, M. E., Kerr, J. A., and Rossi, M. J.: Summary of Evaluated Kinetic and Photochemical Data for Atmospheric Chemistry, IUPAC Subcommittee on Gas Kinetic Data Evaluation for Atmospheric Chemistry, Centre for Atmospheric Science, University of Cambridge, UK, 2006.

Bertram, T. H. and Thornton, J. A.: Toward a general parameterization of $N_2O_5$ reactivity on aqueous particles: the competing effects of particle liquid water, nitrate and chloride, Atmospheric Chemistry and Physics, 9, 8351–8363, https://doi.org/10.5194/acp-9-8351-2009, 2009.

Bi, C., Krechmer, J. E., Frazier, G. O., Xu, W., Lambe, A. T., Claflin, M. S., Lerner, B. M., Jayne, J. T., Worsnop, D. R., Canagaratna, M. R., and Isaacman-VanWertz, G.: Quantification of isomer-resolved iodide chemical ionization mass spectrometry sensitivity and uncertainty using a voltage-scanning approach, Atmospheric Measurement Techniques, 14, 6835–6850, https://doi.org/10.5194/amt-14-6835-2021, 2021.

Bruns, E. A., Krapf, M., Orasche, J., Huang, Y., Zimmermann, R., Drinovec, L., Močnik, G., El-Haddad, I., Slowik, J. G., Dommen, J., Baltensperger, U., and Prévôt, A. S. H.: Characterization of primary and secondary wood combustion products generated under different burner loads, Atmospheric Chemistry and Physics, 15, 2825–2841, https://doi.org/10.5194/acp-15-2825-2015, 2015.

Dörich, R., Eger, P., Lelieveld, J., and Crowley, J. N.: Iodide CIMS and *m/z* 62: the detection of $HNO_3$ as $NO_3^-$ in the presence of PAN, peroxyacetic acid and ozone, Atmospheric Measurement Techniques, 14, 5319–5332, https://doi.org/10.5194/amt-14-5319-2021, 2021.

Evans, M. J. and Jacob, D. J.: Impact of new laboratory studies of $N_2O_5$ hydrolysis on global model budgets of tropospheric nitrogen oxides, ozone, and OH, Geophysical Research Letters, 32, https://doi.org/10.1029/2005GL022469, 2005.

Finlayson-Pitts, B. J. and Pitts, J. N.: Spectroscopy and Photochemistry Fundamentals, in: Chemistry of the Upper and Lower Atmosphere, Elsevier, San Diego, San Francisco, New York, Boston, London, Sydney, Tokyo, 2000.

Gysel, M., Crosier, J., Topping, D. O., Whitehead, J. D., Bower, K. N., Cubison, M. J., Williams, P. I., Flynn, M. J., McFiggans, G. B., and Coe, H.: Closure study between chemical composition and hygroscopic growth of aerosol particles during TORCH2, Atmospheric Chemistry and Physics, 7, 6131–6144, https://doi.org/10.5194/acp-7-6131-2007, 2007.

Haslett, S. L., Taylor, J. W., Deetz, K., Vogel, B., Babić, K., Kalthoff, N., Wieser, A., Dione, C., Lohou, F., Brito, J., Dupuy, R., Schwarzenboeck, A., Zieger, P., and Coe, H.: The radiative impact of out-of-cloud aerosol hygroscopic growth during the summer monsoon in southern West Africa, Atmospheric Chemistry and Physics, 19, 1505–1520, https://doi.org/10.5194/acp-19-1505-2019, 2019.

Huey, L. G., Hanson, D. R., and Howard, C. J.: Reactions of SF6- and I- with Atmospheric Trace Gases, J. Phys. Chem., 99, 5001–5008, 1995.

Kercher, J. P., Riedel, T. P., and Thornton, J. A.: Chlorine activation by $N_2O_5$: simultaneous, in situ detection of $ClNO_2$ and $N_2O_5$ by chemical ionization mass spectrometry, Atmospheric Measurement Techniques, 2, 193–204, https://doi.org/10.5194/amt-2-193-2009, 2009.

Lee, B. H., Lopez-Hilfiker, F. D., Mohr, C., Kurtén, T., Worsnop, D. R., and Thornton, J. A.: An Iodide-Adduct High-Resolution Time-of-Flight Chemical-Ionization Mass Spectrometer: Application to Atmospheric Inorganic and Organic Compounds, Environ. Sci. Technol., 48, 6309–6317, https://doi.org/10.1021/es500362a, 2014.

Lopez-Hilfiker, F. D., Iyer, S., Mohr, C., Lee, B. H., D'Ambro, E. L., Kurtén, T., and Thornton, J. A.: Constraining the sensitivity of iodide adduct chemical ionization mass spectrometry to multifunctional organic molecules using the collision limit and thermodynamic stability of iodide ion adducts, Atmospheric Measurement Techniques, 9, 1505–1512, https://doi.org/10.5194/amt-9-1505-2016, 2016.

Mielke, L. H., Stutz, J., Tsai, C., Hurlock, S. C., Roberts, J. M., Veres, P. R., Froyd, K. D., Hayes, P. L., Cubison, M. J., Jimenez, J. L., Washenfelder, R. A., Young, C. J., Gilman, J. B., de Gouw, J. A., Flynn, J. H., Grossberg, N., Lefer, B. L., Liu, J., Weber, R. J., and Osthoff, H. D.: Heterogeneous formation of nitryl chloride and its role as a nocturnal NOx reservoir species during CalNex-LA 2010, Journal of Geophysical Research: Atmospheres, 118, 10,638-10,652, https://doi.org/10.1002/jgrd.50783, 2013.

Petters, M. D. and Kreidenweis, S. M.: A single parameter representation of hygroscopic growth and cloud condensation nucleus activity, Atmospheric Chemistry and Physics, 7, 1961–1971, https://doi.org/10.5194/acp-7-1961-2007, 2007.

Platt, S. M., Haddad, I. E., Pieber, S. M., Huang, R.-J., Zardini, A. A., Clairotte, M., Suarez-Bertoa, R., Barmet, P., Pfaffenberger, L., Wolf, R., Slowik, J. G., Fuller, S. J., Kalberer, M., Chirico, R., Dommen, J., Astorga, C., Zimmermann, R., Marchand, N., Hellebust, S., Temime-Roussel, B., Baltensperger, U., and Prévôt, A. S. H.: Two-stroke scooters are a dominant source of air pollution in many cities, Nature Communications, 5, 3749, https://doi.org/10.1038/ncomms4749, 2014.

Platt, S. M., Haddad, I. E., Pieber, S. M., Zardini, A. A., Suarez-Bertoa, R., Clairotte, M., Daellenbach, K. R., Huang, R.-J., Slowik, J. G., Hellebust, S., Temime-Roussel, B., Marchand, N., Gouw, J. de, Jimenez, J. L., Hayes, P. L., Robinson, A. L., Baltensperger, U., Astorga, C., and Prévôt, A. S. H.: Gasoline cars produce more carbonaceous particulate matter than modern filter-equipped diesel cars, Scientific Reports, 7, 4926, https://doi.org/10.1038/s41598-017-03714-9, 2017.

Riedel, T. P., Bertram, T. H., Ryder, O. S., Liu, S., Day, D. A., Russell, L. M., Gaston, C. J., Prather, K. A., and Thornton, J. A.: Direct $N_2O_5$ reactivity measurements at a polluted coastal site, Atmospheric Chemistry and Physics, 12, 2959–2968, https://doi.org/10.5194/acp-12-2959-2012, 2012.

Srivastava, A. and Jain, V. K.: Size distribution and source identification of total suspended particulate matter and associated heavy metals in the urban atmosphere of Delhi, Chemosphere, 68, 579–589, https://doi.org/10.1016/j.chemosphere.2006.12.046, 2007.

Tham, Y. J., Wang, Z., Li, Q., Yun, H., Wang, W., Wang, X., Xue, L., Lu, K., Ma, N., Bohn, B., Li, X., Kecorius, S., Größ, J., Shao, M., Wiedensohler, A., Zhang, Y., and Wang, T.: Significant concentrations of nitryl chloride sustained in the morning: investigations of the causes and impacts on ozone production in a polluted region of northern China, Atmospheric Chemistry and Physics, 16, 14959–14977, https://doi.org/10.5194/acp-16-14959-2016, 2016.

Tham, Y. J., Wang, Z., Li, Q., Wang, W., Wang, X., Lu, K., Ma, N., Yan, C., Kecorius, S., Wiedensohler, A., Zhang, Y., and Wang, T.: Heterogeneous $N_2O_5$ uptake coefficient and production yield of $ClNO_2$ in polluted northern China: roles of aerosol water content and chemical composition, Atmospheric Chemistry and Physics, 18, 13155–13171, https://doi.org/10.5194/acp-18-13155-2018, 2018.

Thornton, J. A. and Abbatt, J. P. D.: N2O5 Reaction on Submicron Sea Salt Aerosol: Kinetics, Products, and the Effect of Surface Active Organics, J. Phys. Chem. A, 109, 10004–10012, https://doi.org/10.1021/jp054183t, 2005.

Wang, Z., Wang, W., Tham, Y. J., Li, Q., Wang, H., Wen, L., Wang, X., and Wang, T.: Fast heterogeneous $N_2O_5$ uptake and $ClNO_2$ production in power plant and industrial plumes observed in the nocturnal residual layer over the North China Plain, Atmospheric Chemistry and Physics, 17, 12361–12378, https://doi.org/10.5194/acp-17-12361-2017, 2017.

Xia, M., Wang, W., Wang, Z., Gao, J., Li, H., Liang, Y., Yu, C., Zhang, Y., Wang, P., Zhang, Y., Bi, F., Cheng, X., and Wang, T.: Heterogeneous Uptake of N2O5 in Sand Dust and Urban Aerosols Observed during the Dry Season in Beijing, Atmosphere, 10, 204, https://doi.org/10.3390/atmos10040204, 2019.

Yan, C., Tham, Y. J., Zha, Q., Wang, X., Xue, L., Dai, J., Wang, Z., and Wang, T.: Fast heterogeneous loss of N2O5 leads to significant nighttime NOx removal and nitrate aerosol formation at a coastal background environment of southern China, Science of The Total Environment, 677, 637–647, https://doi.org/10.1016/j.scitotenv.2019.04.389, 2019.

Zhou, W., Zhao, J., Ouyang, B., Mehra, A., Xu, W., Wang, Y., Bannan, T. J., Worrall, S. D., Priestley, M., Bacak, A., Chen, Q., Xie, C., Wang, Q., Wang, J., Du, W., Zhang, Y., Ge, X., Ye, P., Lee, J. D., Fu, P., Wang, Z., Worsnop, D., Jones, R., Percival, C. J., Coe, H., and Sun, Y.: Production of $N_2O_5$ and $ClNO_2$ in summer in urban Beijing, China, Atmospheric Chemistry and Physics, 18, 11581–11597, https://doi.org/10.5194/acp-18-11581-2018, 2018.